Optics & Laser Technology 168 (2024) 109953

Contents lists available at ScienceDirect

Optics and Laser Technology

journal homepage: www.elsevier.com/locate/optlastec

Full length article

Fiber-optic semi-distributed Fabry-Perot interferometer for low-limit label-free detection of CCL5 cancer biomarker

Aida Rakhimbekova [a], Kuanysh Seitkamal [b], Baizak Kudaibergenov [a,b], Faisal Nazir [c], Tri Pham [c], Wilfried Blanc [d], Luca Vangelista [b,e], Daniele Tosi [a,f,*]

[a] Department of Electrical and Computer Engineering, School of Engineering and Digital Sciences, Nazarbayev University, Astana, Kazakhstan
[b] Department of Biomedical Sciences, School of Medicine, Nazarbayev University, Astana, Kazakhstan
[c] Department of Biology, School of Sciences and Humanities, Nazarbayev University, Astana, Kazakhstan
[d] Université Côte d'Azur, INPHYNI, CNRS UMR7010, 17 rue Julien Lauprètre, 06200 Nice, France
[e] Department of Molecular Medicine, University of Pavia, Pavia, Italy
[f] Laboratory of Biosensors and Bioinstruments, National Laboratory Astana, Astana, Kazakhstan

ARTICLE INFO

Keywords:
Optical fiber biosensors
Single-mode fibers
Fabry-Perot interferometry
Enhanced Rayleigh backscattering
CCL5
Cancer biomarker detection

ABSTRACT

We present an optical fiber label-free biosensor based on a partially stochastic Fabry-Perot interferometer for the detection of CCL5 (CC Chemokine Ligand 5) cancer biomarker. The sensor has a very simple fabrication process, with a splice-and-cleave approach that requires only one splice and a subsequent cleave at the fiber tip. The enhanced backscattering within the Mg-NP fiber paired with the Fresnel reflection at the fiber tip forms a low-finesse interferometric structure; the inner reflections due to Rayleigh scattering provide an additional layers of phase shifts, forming a semi-distributed interferometer (SDI). The average sensitivity of the SDI sensors has been reported to be 92.5 dB/RIU. Sensors were biofunctionalized for the purpose of detecting CCL5 by means of a silanization process. We report the detection of CCL5 in diluted serum with a sensitivity of 2.947 mRIU for each 10-fold concentration increase and a limit of detection of 17.6 aM.

1. Introduction

1.1. Biosensors for cancer biomarker detection

The enzyme-linked immunosorbent assay (ELISA) is the most commonly used method for biomarker detection and quantification in biological samples in routine clinical diagnostics. ELISA methods are based on the principle of a solid phase enzyme-linked immunosorbent assay using colorimetric or fluorescent readout signals for visual detection of cancer biomarkers [1]. In parallel to immunoassays, real-time operating biosensors are shifting the cancer biomarker detection paradigm to a rapid diagnostic procedure, building on both labeled and label-free methods that exploit the capability to detect changes in the biological samples (such as blood, saliva or urine) and a bio-functionalization process that enhances the specificity.

Within this technological challenge, optical fiber biosensors are playing a significant role in modern devices for the detection of cancer biomarkers [2] because they enable real-time detection and the possibility for *in situ* diagnostic. Due to their small size and light weight, these biosensors can be included in medical devices such as catheters [3], endoscopic probes [4], or subcutaneous sensors [5].

One important class of optical fiber biosensors makes use of large-core, multimode fibers (MMFs) operating at visible wavelengths and using UV–VIS spectrometers as detectors [6]. Common approaches rely on surface plasmon resonance [7], U-bent fibers [8], or a simple interrogation of Fresnel reflectivity at the fiber end [9]. For this reason, MMF fibers are therefore commonly employed in low-cost fiber optic systems, including smartphone hardware [10]. MMF-based biosensors, however, have two main drawbacks when used in precision and low-limit diagnostic: 1) the presence of a large number of weakly confined modes makes the sensing systems sensitive to power fluctuations and vulnerable to the effects of fiber bending because the fiber hosts numerous modes (in the order of several thousand up to a few million); and 2) most of the sensing approaches require the light to be transmitted through the sensing region, whereas *in situ* sensing requires a single reflective probe [11].

* Corresponding author at: Department of Electrical and Computer Engineering, School of Engineering and Digital Sciences, Nazarbayev University, Astana, Kazakhstan.
E-mail address: daniele.tosi@nu.edu.kz (D. Tosi).

https://doi.org/10.1016/j.optlastec.2023.109953
Received 18 May 2023; Received in revised form 4 August 2023; Accepted 14 August 2023
Available online 19 August 2023

For this reason, modern approaches for sensing have relied on telecom-grade single-mode fibers (SMFs). Since all the light is propagated with a single well-confined mode and therefore is traveling with the same effective refractive index, SMF-based biosensors have a much better stability and power handling. In addition, telecom-grade hardware can be used, having a much narrower spectral or power resolution. The two main architectures based on SMF biosensors rely on special fiber Bragg gratings (FBGs), and in-fiber interferometers. Grating-based biosensors such as tilted FBG [12] and long-period gratings [13], also employed in biochemical sensing [14–16]. excite cladding modes within the fiber structure. These biosensors also have the same problems of MMF-based biosensors because the fiber cladding is a multi-mode guiding structure [17]. On the other side, interferometers can achieve high performance [18], and can be implemented through micro-fabrications [19], as reported in [20] for DNA sensing and in [21] for HER2 cancer biomarker detection. However, the fabrication process for interferometers is quite cumbersome and cannot be easily automated. The realization of a SMF-based low-cost, reflective biosensor with an entirely automated fabrication process is still an open challenge.

In order to reduce the fabrication complexity and enable low-cost sensing units for the detection of cancer biomarkers, minimalistic approaches with a one- or two-step fabrication process leading to sensors with a quasi-random reflection spectrum have been proposed [22]. A first approach of this kind consists of a fiber-tip ball resonator, which has been reported for the detection of CD44 cancer biomarkers [23]. Other strategies rely on reflector-less biosensors, which are accomplished by etching or tapering an optical fiber to increase the evanescent wave profile.

1.2. The proposed semi-distributed fiber-optic interferometer

In this paper, we take a further step towards fabrication simplicity by introducing a reflecting probe that only requires two operations: a SMF-SMF splice performed with a telecom splicer, and a fiber cleave at the tip. We refer to this method as “splice-and-cleave” for this reason. The structure is formed by using an unconventional sensing fiber, doped with Mg-silicate nanoparticles (Mg-NP) in its core [24]. Fig. 1 shows a schematic illustration of the use of Mg-NP doped fiber in biosensing. Although the entire fiber can be used in biophysical sensing of temperature or shape in medical devices [25], earlier work has described the use of such fiber in reflector-less biosensors, in which no reflective elements are used and only the enhanced Rayleigh backscattering is needed for sensing. This has first been reported using an etched structure [26], and more recently with a fiber taper [27]. Both of these structures have been used to detect biomarkers, and they both require the fabrication of a sensing probe using either wet-etching in hydrofluoric acid or tapering a fiber with a CO_2 laser splicer.

The approach proposed in this paper converts the Mg-NP fiber into a splice-and-cleave semi-distributed interferometer (SDI). The interface between the SMF and the Mg-NP fiber acts as a weak mirror, with a second mirror obtained on the fiber tip; this forms a Fabry-Perot cavity with deterministic properties. Due to the randomly distributed reflections within the Mg-NP, we get a continuous collection of reflections with random patterns as the density of the scattering centers fluctuates throughout the fiber profile, resulting in a stochastic set of mirrors. The resulting SDI structure combines the deterministic and stochastic properties to create a low-finesse interferometer with well-defined modes and average sensitivity of 92.5 dB/RIU (refractive index units). Given that both splice-cleave operations can be completed on a typical telecom splicer in less than a minute, this is the simplest fabrication of an interferometric sensor to date. Additionally, the detection limit is improved because the SDI is extremely sensitive and telecom-grade hardware has higher accuracy than UV–VIS spectral analyzers.

1.3. Significance of CCL5 as a biomarker

The proposed SDI sensor has been functionalized for the detection of a cancer biomarker with increasing impact for diagnostic applications. The concept of using cytokines as biomarkers for early diagnosis and surveillance of various diseases has recently attracted a lot of attention in the literature. Chemokines coordinate leukocyte migration to control immune responses against cancer [29]. CC chemokine ligand 5 (CCL5) facilitates the migration of T cells and monocytes to areas of tissue injury. Hence, the inflammatory insult can induce the expression of CCL5. CCL5 is expressed by tumor cells in addition to T lymphocytes, macrophages, eosinophils and platelets [30]. Certain types of tumors have been linked to the overexpression of CCL5, which in turn accelerates tumor growth, improves tumor cell motility, and stimulates angiogenesis [31].

Additionally, CCL5 is becoming a more vital biomarker in the early diagnosis and monitoring of a number of cancers, such as breast cancer [32], lung cancer [33], prostate cancer [34], pancreatic cancer [35], esophageal cancer [36] and gastric cancer [31]. CCL5 serum levels range from 13 ng/mL [37] to 35 ng/mL [38] in healthy individuals, but they can rise to a mean of 66 ng/ml in cancer patients [39]. Overall, there was a substantial difference in the serum levels of CCL5 in cancer patients and healthy controls. As a result, the expression of CCL5 by cancer cells and the presence of the protein in serum may signify that the illness is developing and becoming more debilitating [40].

CCL5 is the major ligand of CCR5, a chemokine receptor of considerable relevance in pathology, from HIV-1 to atherosclerosis, and the CCL5:CCR5 axis is indeed central to cancer [41].

ELISA-based techniques and immunoassays have been used to analyze CCL5 in human bodily fluids, specifically plasma or serum. The

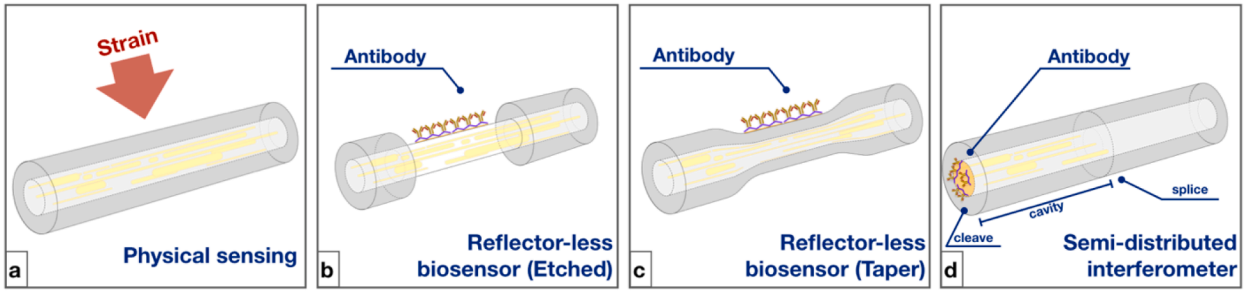

Fig. 1. Details of the structure of MgO-NP fiber-based sensors for biomedical applications. The proposed semi-distributed interferometer design is depicted in the schematic alongside the architectures that were previously published. (a) The MgO-NP stand-alone fiber has been implemented in physical sensing, including shape detection [25] and temperature changes [28] in medical devices. The design of this structure was subsequently modified to create reflector-less biosensors by enhancing the evanescent fields. The proposed designs are based on (b) etching [26], and (c) shallow-tapering [27] MgO-NP fiber. (d) The proposed semi-distributed interferometer enhances the ease of the biosensor fabrication by taking advantage of the tiny reflectivity at the SMF/MgO-NP interface to create a second mirror through straightforward fiber cleaving, forming a cavity interleaved by the partially reflective fiber cross-section.

detection principle of this method is based on complexing antibodies and antigens to produce a measurable result [42]. Despite the advancements in the use of ELISA-based technologies for protein detection, many drawbacks remain. For instance, ELISA-based procedures have limited throughput, require a lot of samples for various analyses, and present difficulties for point-of-care diagnostics [43]. The majority of commercially available HRP/TMB-based (3,3′,5,5′-Tetramethylbenzidine - horseradish peroxidase) colorimetric ELISA kits have detection limits of approximately 2 pg/mL, encompassing a broad range of values (0.94 pg/mL – 2000 pg/mL).

2. Materials and methods

2.1. Materials

SDS – PAGE was performed on BioRad equipment (Hercules, California, United States) with a Tris-Glycine-SDS running buffer serving as the electrolyte: 1.9 M Glycine, 0.25 M tris(hydroxymethyl)aminomethane (TRIS) base, and 0.03 M SDS, pH 8.3. Protein samples were separated into 0.75 mm thick gels with 15% acrylamide. PageRuler™ Plus Prestained Protein Ladder (Thermo Scientific™) was used as a molecular weight marker. Electrophoresis was conducted at 150 V. The membranes for the Western Blotting were incubated overnight with polyclonal Rabbit anti-Human RANTES (CCL5) antibody (Peprotech) diluted to 1:1000 in TBS 1X buffer + 0.1 % Tween 20 containing 3% BSA (Sigma-Aldrich). Goat anti-rabbit IgG horseradish peroxidase-conjugated antibodies (Sigma-Aldrich) diluted to 1:5000 in TBS 1X buffer + 0.1 % Tween 20 containing 5% dry milk solution were used as secondary antibodies.

SMF (SMF-28e+), sucrose, 70% sulfuric acid: 30 % hydrogen peroxide, 3-aminopropyl trimethoxysilane (APTMS), methanol, glutaraldehyde, BSA, Phosphate buffered saline (PBS) and Human serum (HS), 1 ml (Bioject® Budget 100 IU insulin), venous catheter (size G16).

2.2. Working principle of the biosensor

See Supplementary Materials, section A.

2.3. Fabrication of the sensors

The schematic, fabrication and functionalization processes for the SDI biosensor for the label-free detection of CCL5 are shown in Fig. 2.

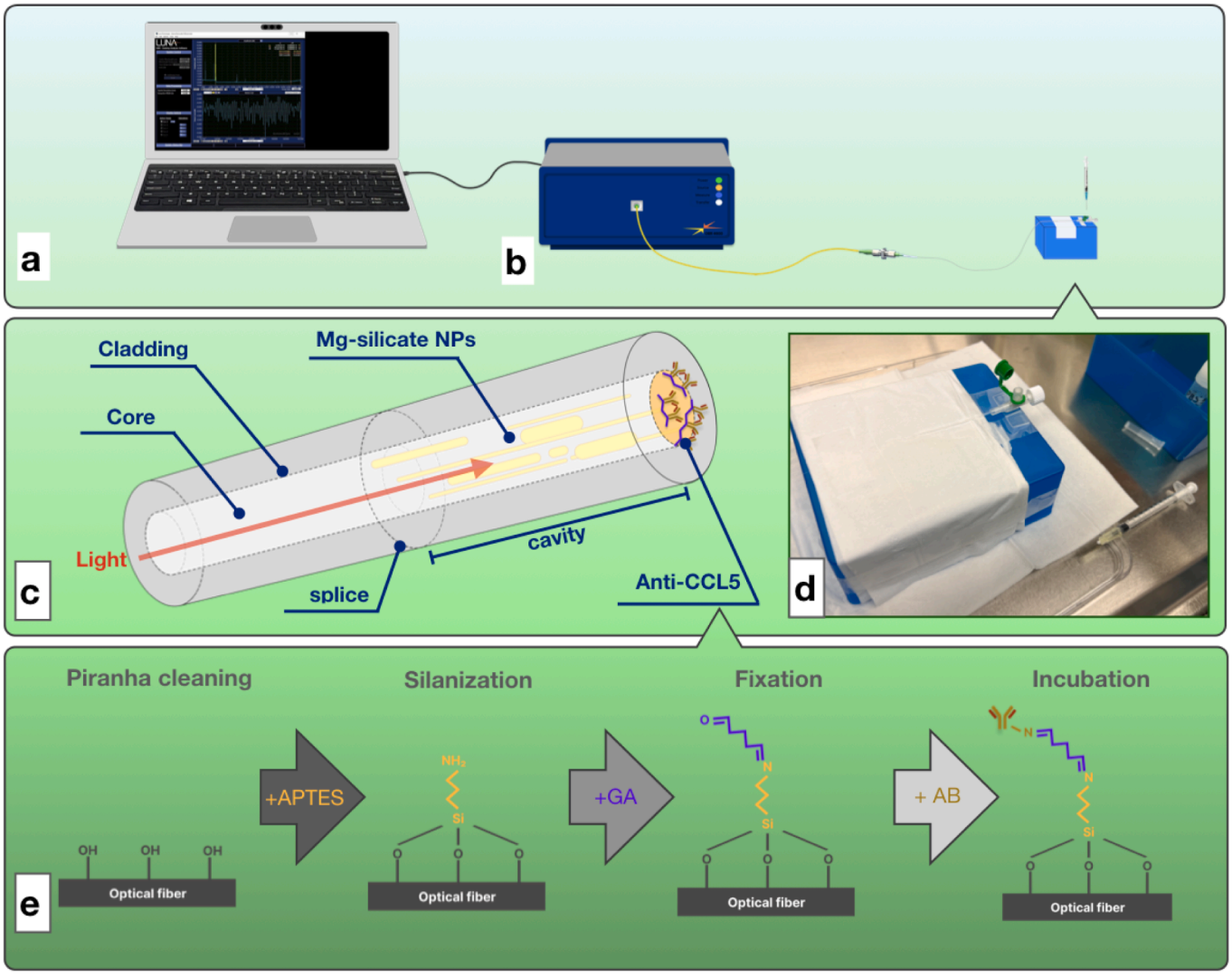

Fig. 2. Fabrication, interrogation, and biofunctionalization process for a semi-distributed interferometer label-free sensor for CCL5 detection. (a-b) The setup used for the interrogation, employing (b) an OBR instrument for the interrogation with a SMF fiber output and (a) data acquisition via dedicated software. (c) Schematic of the biosensor, showing the cavity formed with two mirrors at the tip and at distal side (SMF/Mg-NP interface). (d) Photograph of the OBR hardware and sensing system. (e) Biofunctionalization process, highlighting the piranha cleaning, silanization, fixation, and incubation steps.

The fabrication of the Mg-NP fibers was carried out as follows. The preform was fabricated by the conventional MCVD (Modified Chemical Vapor Deposition) technique [44]. A germanosilicate porous layer was deposited inside an F300 silica tube (Heraeus, Germany) with external and internal diameters of 20 and 17 mm, respectively. 0.1 M of $MgCl_2$ and 10^{-4} M of $ErCl_3$ were dissolved in ethanol to prepare the doping solution. Magnesium was added to trigger the formation of Mg-silicate nanoparticles by phase separation [45]. A non-conventional solution doping method was used to dope the core's porous layer. The doping solution (5 ml) was injected into the horizontally rotating tube and then dried at room temperature with an oxygen gas flow. This step was repeated three times (total amount of doping solution injected: 15 ml). The porous layer then was sintered and the tube was collapsed into a preform by heating above 2000 °C. The diameter of the preform was kept around 10 mm. Optical fiber was finally produced on a drawing tower by heating the preform to approximately 2100 °C. This step induces an elongation of the nanoparticles [46]. The fiber has a 125 μm diameter with a 10 μm core. The refractive index difference between the core and the cladding has been measured using a Photon Kinetics S14 and was estimated to be 10^{-2}. Based on EDX analyses, the highest Mg and Ge concentrations are 1.7 and 0.3 at%, respectively. In the fiber, the largest nanoparticle diameter (in the transverse section) is about 100 nm. A Rayleigh backscattering profile is reported in Supplementary Material.

Regarding the SDI fabrication, a SMF fiber was spliced to the Mg-NP fiber; by using the optical backscatter reflectometer (OBR), the exact location of the Mg-NP fiber corresponding to the reflection peak was identified. Then the sensor was cleaved on the fiber tip side leaving a part of Mg-NP fiber, corresponding to the Fabry-Perot cavity, having length < 1 mm. The whole fabrication process requires ≤ 2 min to the operator; it is mostly dedicated to the SMF/Mg-NP splice, which is a process that however is common to most of the other optical biosensors such as gratings or interferometers (which also require to be spliced), while the OBR scan and cleave require less than 30 s. All the sensors reported in this work have been fabricated using this method.

All sensors were calibrated in order to measure the response to the surrounding refractive index (RI). The calibration method is similar to the one reported in [23]. Each sensor was exposed to different RI values, starting with a solution of 6 ml of 10% sucrose, and then increasing by 200 μL of 40% sucrose in each step until the solution reaches 1 ml (RI = 1.34866 to 1.35186) were calibrated using an Abbemat 3000 refractometer. Given the narrow RI range (ΔRI = 3.2 mRIU), we used a linear small-signal approximation verifying that the regression has coefficient of determination $R^2 \geq 0.95$.

2.4. Surface biofunctionalization

The surface of the fabricated SDI was cleaned by immersing it in a solution of 70% sulfuric acid and 30% hydrogen peroxide for 15 min to remove organic contaminants and activate the surface [47]. It was then washed with deionized water and dried in the air. The cleaned surface was then treated with a solution of 5% 3-aminopropyl trimethoxysilane in methanol for 90 min. The silanized region was then washed with methanol and water and baked in an oven at 80–90 °C for 30 min to eliminate solvents and promote cross-linking. The surface was then treated with a solution of 2.5% glutaraldehyde in PBS for 2 h in order to attach anti-CCL5 antibodies onto the fiber surface next in the concentration of 34 μg/mL. The surface was then rinsed with PBS and incubated in an antibody solution at 4 °C overnight [23]. The next day, the surface was rinsed again with PBS to remove unbound antibodies, blocked with 1% BSA for 30 min, and rinsed with PBS again before being used for protein detection.

2.5. Interrogation of the fiber-optic probe

The interrogation of the sensors has been performed using an optical backscatter reflectometer (Luna OBR4600, Luna Inc.), operating in frequency mode. The instrument was set to scan the spectrum over 1527–1613 nm with 1 GHz resolution bandwidth and no gain; spectral data were filtered with a low-pass digital filter (Butterworth, 5th order, 0.1 cut-off). The spectral intensity analysis was carried out by using a second-order polynomial fit to estimate the peak/valley intensity levels. Since the SDI probes have an interferometer-shaped spectrum, we show the spectral peak for each measurement that displays the most consistent response among the high-sensitivity spectral peaks.

2.6. CCL5 detection and specificity analysis

The functionalized SDI sensors were used to detect CCL5 in PBS and HS 10%. The free end of the sensor was placed inside a venous catheter, where a solution of PBS or FBS containing the antigens with specified concentration was injected using a 1 ml syringe with a 30Gx½ needle. The solution was incubated for 10 min at room temperature, while the changes were measured every minute by OBR. The protein concentration range was from 1 aM to 10 nM and it was increased by a factor of 10 for each step. The signal was recorded under stable and quiet conditions, to prevent any disturbances in measurement as the sensor is very sensitive to vibrations. In order to account for the different sensitivities, the response of the sensor was normalized by the RI sensitivity.

The specificity test was conducted to evaluate the performance of the sensor in detecting CCL5 in presence of unrelated proteins (IL4 and thrombin). Samples containing identical concentrations of each protein were sequentially injected into a venous catheter equipped with a sensor at 10-minute intervals in the following order: thrombin, IL4, and CCL5. The sensor was washed with PBS before the measurement.

2.7. Surface morphology analysis

Atomic force microscope (JPK NanoWizard 4XP, Bruker Instruments Germany) was used to image the surface morphology of the biosensor after each functionalization step using a super sharp probe NSG30_SS (NT-MDT, USA). The sensing tip had calibrated spring constant K = 26 N/m, resonant frequency f = 300 kHz, and typical tip curvature radius r = 2 nm. All images were acquired in the air at room temperature operating in PeakForce Tapping® mode at 1 μm^2 scan size with a resolution of 5 nm/pixel. All images were processed with JPK-Data processing application and the root mean square (RMS) roughness was obtained. Gwyddion software was used to generate three-dimensional (3D) images for visualization of the surface roughness. For each surface functionalization phase including the bare biosensor, three separate samples were prepared and imaged, each with at least 10 different sites for statistical analysis. To assess the statistical significance of changes in the surface roughness between various phases, statistical tests were conducted using GraphPad Prism 9 (see Statistical analysis section in the Supplementary Materials).

3. Results

3.1. Spectral analysis and refractive index detection

We report in Fig. 3 the spectrum of a semi-distributed interferometer, obtained through a cavity with an estimated length of ~ 0.35 mm. We observe that the spectral fingerprint resembles a low-finesse interferometer [48], with reflectivity values around −30 dB and free spectral range (FSR), defined as the wavelength difference between two adjacent peaks or valleys, equal to 2.5 nm at 1550 nm. The fringe visibility of the interferometer is about 0.08. The reflection spectrum corresponds to the semi-stochastic configuration of the SDI sensor: while the spectral envelope has the waveform of a classical interferometer with a well-defined FSR, the inner spectral levels appear to fluctuate due to the strong reflections occurring within the Mg-NP fiber. The sensor combines a stochastic part (due to the stochastic nature of the nanoparticles

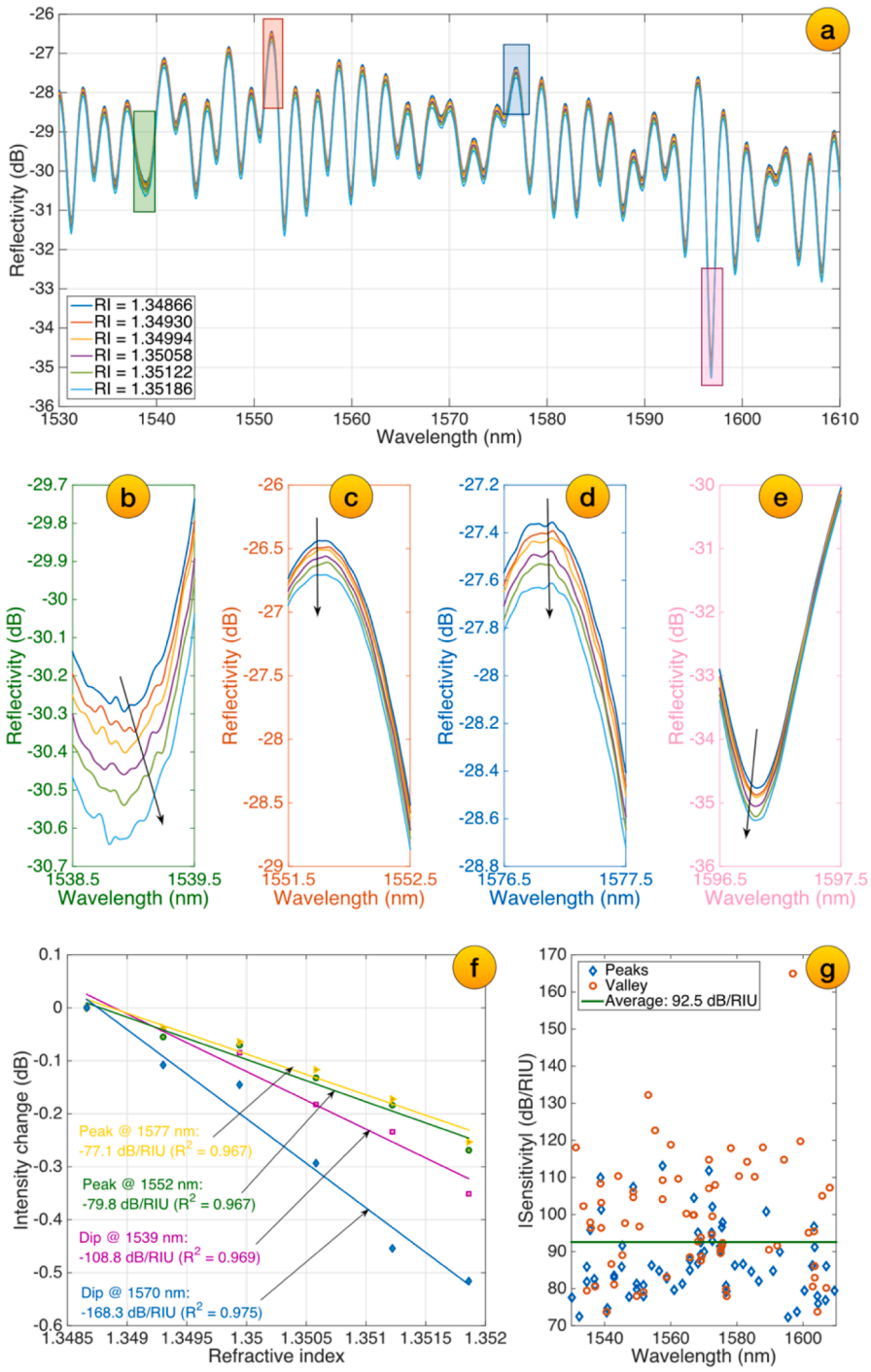

Fig. 3. Spectral characteristics and refractive index sensitivity of the semi-distributed interferometer. (a) Reflection spectrum of the SDI biosensor, acquired for different values of refractive index ranging from 1.34866 to 1.35186. (b-e) Insets show the behavior of the sensor in correspondence with several spectral dips or peaks, at (b) 1539 nm, (c) 1552 nm, (d) 1577 nm, (e) 1597 nm; each chart shows the response of the sensor over a 1-nm wavelength window. (f) Refractive index sensitivity reporting the estimated intensity change for the four modes selected and displayed in the (b-e) insets; the sensitivity has been estimated through linear regression with R^2 coefficient > 0.96. (g) Estimation of the sensitivity (absolute values) for each mode, reporting the recorded values for spectral peaks (blue markers) and spectral valleys (red markers).

size and distributions within each fiber cross-section), and a deterministic part (the reflections at the fiber tip and the distal side of the interferometer, which can be measured). The backscattering trace, supplied in Supplementary Data (Figure S6) shows that the reflectivity occurring at the SMF/Mg-NP interface is 10^{-5} while an ideal Fresnel reflection yields a reflectivity of 1.4 10^{-3}.

The RI sensitivity is encoded in each spectral peak/valley, as each RI increment causes a reduction of the mirror reflectivity on the fiber tip. This can be evaluated by tracking the intensity change for each mode as a function of each RI value; the intensity levels have been estimated using a second-order fit with the method reported in [49]. The intensity drops for any peak or valley, as shown in Fig. 3(b-e); by means of linear regression, the sensitivity for each spectral feature can be estimated, ranging from 77.1 to 168.3 dB/RIU.

Since the sensitivity appears to vary as a function of the investigated spectral feature, in Fig. 3(f) we report the experimentally obtained sensitivity for each peak or valley within the SDI spectrum; all features reported in the chart have $R^2 > 0.95$. The average value of the sensitivity is 92.5 dB/RIU, with a standard deviation of 14.5 dB/RIU. We observe that in general, the sensitivity is higher for spectral dips (mean: 98.2 dB/RIU, standard deviation: 15.9 dB/RIU) and lower for spectral peaks (mean: 86.8 dB/RIU, standard deviation: 10.1 dB/RIU). The RI sensitivity reported for this sensor is similar to the value reported for fiber-optic ball resonators [23], which also track the intensity change of the

spectral envelope with an OBR instrument, and has shown attomolar-level detection limits for proteins sensing.

Similar behavior was observed for multiple SDI sensors that have been fabricated; the spectra for additional sensors are reported in Supplementary Materials, Figure S7.

3.2. Detection of CCL5 biomarker

Label-free detection of CCL5 has been performed using different sensors, each employed for the detection in PBS or in serum. The detection was performed by stabilizing the measurement for 3 min, and obtaining then 7 consecutive measurements at 1 min sampling time. CCL5 concentrations were taken from 1 aM to 100 nM with a 10-fold increase between each value.

The spectra of the SDI biosensor used for detection in PBS are shown in Fig. 4(a-b); the sensor displays an interferometric pattern with FSR of 2.2 nm and maximum reflectivity close to −30 dB. The whole spectrum appears to shift downwards as CCL5 concentration increases. A different sensor was used for the detection in serum, with spectrum shown in Fig. 4(c-d); this SDI biosensor has a FSR equal to 1.1 nm, and a

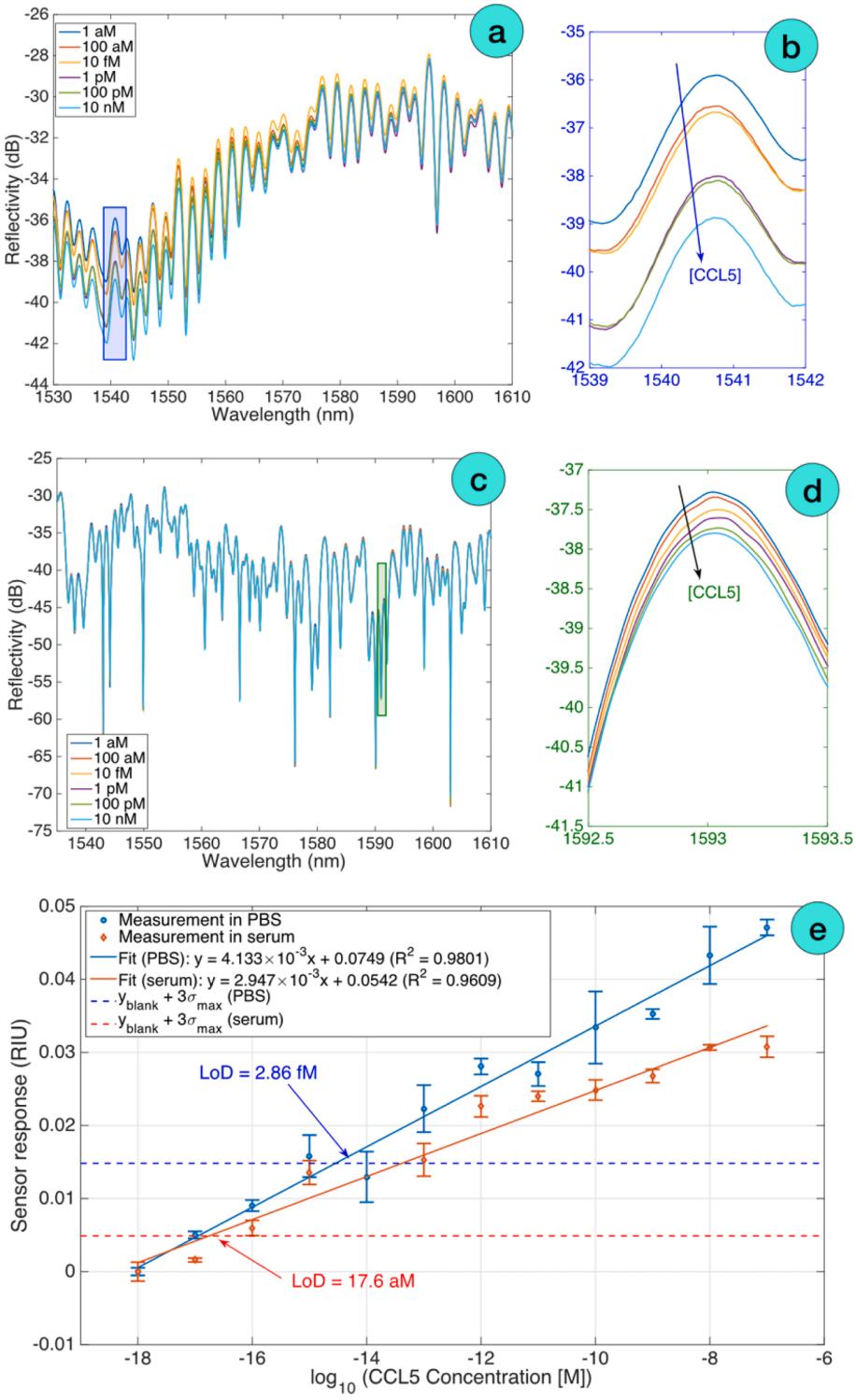

Fig. 4. Label-free detection of CCL5 in PBS and serum through the semi-distributed interferometer. (a) Reflection spectrum of the SDI sensor used for PBS detection, obtained for different CCL5 concentrations; (b) inset showing the spectral peak used for CCL5 detection, around 1541 nm. (c) Reflection spectrum of the SDI sensor used for serum detection, obtained for different CCL5 concentrations; (d) inset showing the spectral peak used for CCL5 detection, around 1593 nm. (e) Detection of CCL5, reporting the output for each sensor for CCL5 concentrations ranging from 1 aM to 100 nM with a 10-fold increase (blue = PBS; red = serum). Data are reported for average (markers) and ± standard deviation (error bars) for 7 consecutive measurements, performed with 1 min sampling time after stabilization for 3 min. The output of each sensor has been normalized by the sensitivity. Log-linear curves have been estimated through linear regression. Horizontal lines correspond to the LoD levels, estimated as 17.6 aM in serum and 2.86 fM in PBS.

reflectivity level of around −35 dB which is lower than the previous sensor possibly due to the quality of the fiber cleave angle on the tip side. In order to account for the different sensitivity of each sensor, and the different peaks that are used for CCL5 detection, the sensor output has been normalized by the sensitivity of each sensor, thus reporting the corresponding change in refractive index units; this process was used for other fiber-optic biosensors previously reported [50]. The sensitivity of the sensor used for the detection in PBS is 74.3 dB/RIU, while the sensor used for serum detection has a sensitivity rating of 24.6 dB/RIU.

The detection of CCL5 at different concentrations is reported in Fig. 4 (e), and is reported for both PBS and serum analytes in terms of average values and error bars (±standard deviation). The response in PBS shows a log-linear trend, with excellent linearity ($R^2 = 0.98$) confirming the typical trend reported for fiber-optic sensors working with the interferometric principle (Ran *et al.* 2021). The sensor is responsive to very low concentrations, exploiting the dense wavelength sampling obtained through the OBR instrument. The sensitivity obtained for this sensor is 4.13 mRIU for each 10x increment of CCL5 concentration. A similar trend was observed for the measurement in serum, obtaining a log-linear pattern ($R^2 = 0.96$) and sensitivity of 2.95 mRIU for each 10-fold protein concentration increase.

The limit of detection (LoD) was estimated using the analytical method reported by (Chiavaioli *et al.* 2017). The method is based on the log-linear fit obtained by regression and reported in Fig. 4(e); the LoD concentration x_{LoD} has been estimated as $x_{LoD} = f^{-1}(y_{blank} + 3\sigma_{max})$ where $y = f(x)$ is the log-linear function relating the concentration change to the sensor output, y_{blank} is the sensor output obtained for the blank sample, and σ_{max} is the maximum of all the standard deviation values obtained for all concentrations.

The LoD was estimated at 17.6 aM in serum, while the value in PBS is 2.86 fM; the fact that the limit is lower in serum is explained by the larger uncertainty that was observed in PBS at 0.1 nM concentration. In any case, the chart clearly displays that the sensor has a detectable response even at concentrations of CCL5 as low as a few tens of attomolar, confirming the capability of this label-free detection method.

In order to assess the repeatability to reproduce different CCL5 sensors, we compared three different sensor outputs (normalized, in order to account for the different sensitivity ratings) and tested them on the same CCL5 concentration range. The results, reported in Figure S9 of Supplementary Materials, show that the level of reproducibility floats between 9% and 26% throughout the intermediate concentrations measured in PBS, confirming the quality of the detection.

The biological performances of the SDI biosensors can be compared with other fiber-optic biosensors based on either interferometers, or

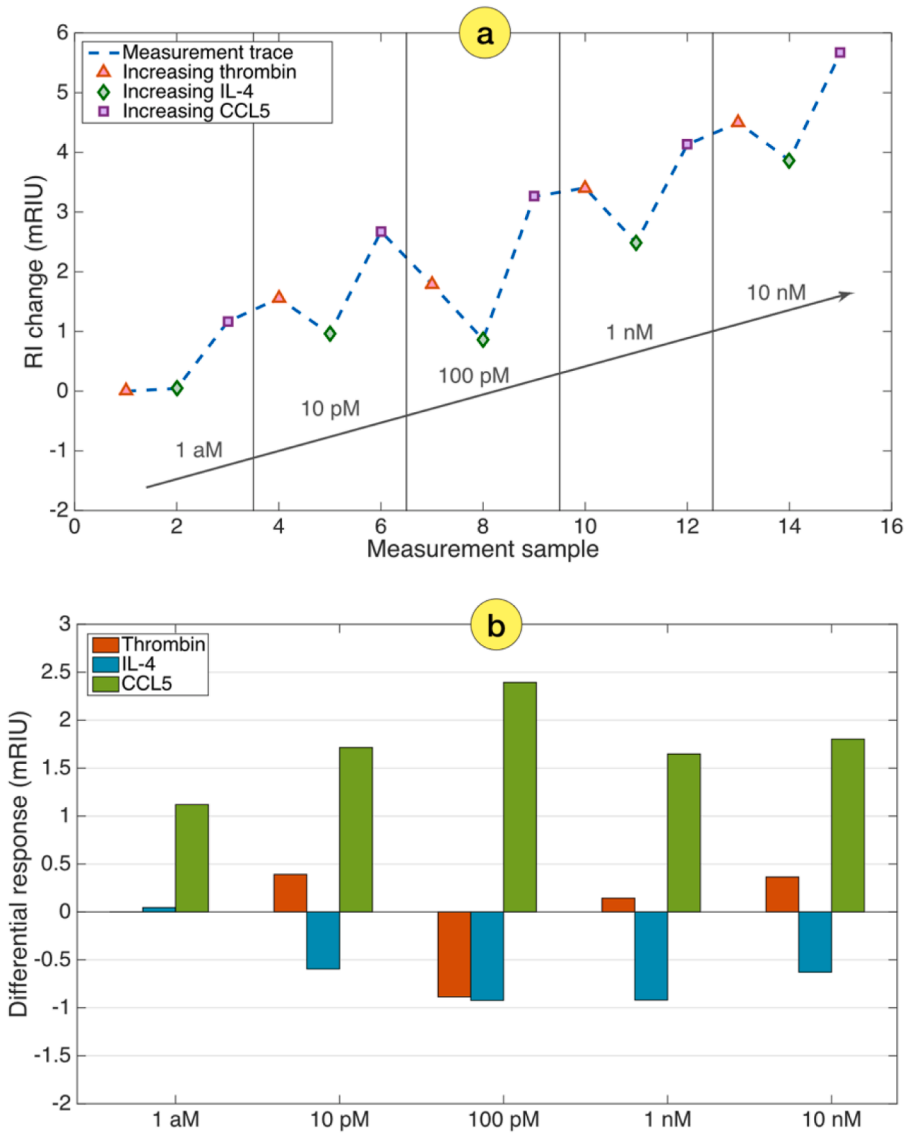

Fig. 5. Analysis of the specificity to CCL5 of the semi-distributed biosensor. (a) Measurement trace, reporting the response of the biosensor to each concentration change. The trace reports the instantaneous response of the sensor (normalized to RIU units), after adding thrombin, IL-4, and then CCL5 in concentrations of 1 aM, 10 pM, 100 pM, 1 nM, and 10 nM respectively. (b) Specificity of the method, reporting the differential response (difference between the previous and current measurement) for each control and main sensor.

other analogous weak reflectors on the fiber tip. The main analogy is with fiber-optic ball resonators, which have been demonstrated for the detection of CD44 biomarker with limit of detection of 4.68 aM in serum using a fiber silanization [23] and 111 fM when using a hybrid functionalization [51], sharing a similar intensity-detection principle. Conversely, interferometers have also been used to detect proteins in serum: the harmonic microfiber cavity reported by Ran *et al.* reported a detection limit of 13.5 ng/mL for the detection of cardiac troponin I biomarker [18], while the Mach-Zehnder on-fiber interferometer proposed by Li *et al.* [52] shows a detection limit of 257 ng/mL for bovine serum aluminum detection. Overall, the LoD levels are comparable, but the SDI probes offers a clear advantage in terms of ease of fabrication.

3.3. Specificity

The specificity of the CCL5 biosensor is shown in Fig. 5, performed

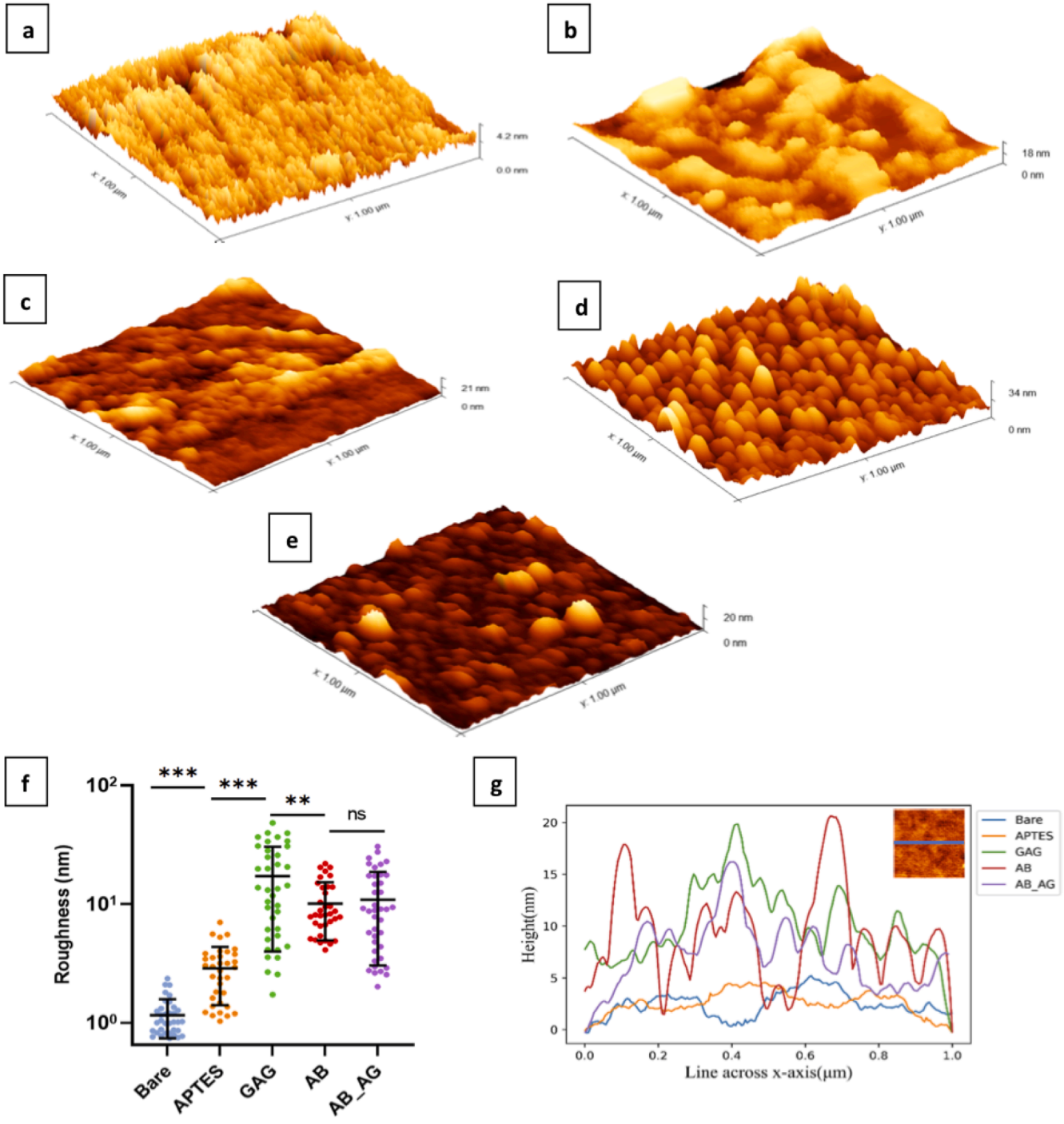

Fig. 6. Surface roughness analysis for unmodified and surface-modified biosensors. 3D images of a 1 µm × 1 µm scanned biosensor surface for the following conditions: (a) bare/untreated sensor, (b) treatment with 3-aminopropyl trimethoxysilane (APTES), (c) further treatment with glutaraldehyde (GAG), (d) immobilization with antibodies (AB), and (e) attachment of CCL5 cancer biomarker to antibodies treated surface (AB_AG). (f) Roughness is statistically compared following each functionalization phase (N >= 35). (g) A typical height profile along a horizontal line in the image. All measurements were performed in air using PeakForce Tapping® mode.

for a SDI sensor biofunctionalized for CCL5. The first chart shows the measurement trace, which has been performed by exposing the functionalized biosensor to increasing concentrations of controls (thrombin, IL4) and then to CCL5 protein. The measurement was performed at 1 aM, 10 pM, 100 pM, 1 nM, and 10 nM repeating the steps. The trace shows that the increments of CCL5 concentration cause a change of the trace ranging between 1.1 10^{-3} RIU to 2.4 10^{-3} RIU; on the other side, concentration increments of the controls contribute to either negative change of the sensor outputs (up to $-0.9\ 10^{-3}$ RIU) or to a small change of the output (up to 0.4 10^{-3} RIU). The second chart shows, in a bar chart, the differential outputs for each incremental step of CCL5 compared to the controls; while CCL5 increments contribute to a positive output (corresponding to the decrease of spectral levels), the thrombin and IL-4 contributions show the opposite sign, and are marginal compared to CCL5 detection. Such behavior was previously obtained for reflector-less biosensors [26]. Overall, the CCL5 detection has a high specificity, as the response to non-specific controls has magnitude ranging from 34.6% at low concentration (10 pM) to 34.8% at the highest concentration (10 nM), while exhibiting a trend with the opposite sign.

3.4. Analysis of the biofunctionalized surface

Fig. 6(a-e) illustrate the surface morphologies of all functionalization phases, including the bare sensor. For all phases of the sensor, the mean and standard error of the mean (SEM) values of the root-mean-square (RMS) roughness are computed and summarized in Table S1. As can be seen, the surface of the bare sensor in Fig. 6(a) is quite smooth, with a measured roughness value of 1.2 ± 0.07 nm. Fig. 6(b) shows how 3-aminopropyl trimethoxysilane (APTES) treatment elevated the sensor's surface roughness to 2.9 ± 0.25 nm. The surface roughness rose to 17 ± 2.10 nm after additional glutaraldehyde (GAG) treatment, as shown in Fig. 6(c). The roughness decreased to 10 ± 0.87 nm after immobilization of anti-CCL5 antibodies (AB), rather than increasing further. This decrease in surface roughness is the result of the surface being conjugated with anti-CCL5 antibodies filling up the valleys created by the APTES treatment and lowering the height difference between the peaks and the troughs on the surface. Antibodies were successfully immobilized on the GAG-functionalized sensor as evidenced by the regularity in the size of spherical micelles seen in Fig. 6(d). Several globular micelles were discovered on the surface of the CCL5-attached sensor (AB_AG), some of which were found to be significantly larger than the micelles for antibodies (see Fig. 6(e)). The outcome further demonstrated that CCL5 were bound to the AB-treated surface after detection. However, as can be shown in Fig. 6(f), the surface roughness after CCL5 attachment only slightly increased and was not noticeably different from that of the AB treated surface. The reason for this insignificant change is that the biosensor is so sensitive that it can detect when just a few CCL5 molecules have attached to the sensor surface (i.e. approximately 5 CCL5 molecules on a 1 μm^2 area), which is not enough to increase the surface roughness of the entire scan region. Fig. 6(g) depicted the representative's height profile along a line drawn through the center of the scan region.

4. Conclusions

We reported the fabrication and biofunctionalization process for a fiber-optic semi-distributed interferometer aimed at the detection of CCL5 cancer biomarker. The sensor has a rapid and simple fabrication process, based only on one splice and one cleave of single-mode fibers. The working principle is routed in the use of high-scattering Mg-nanoparticles doped fibers to increase Rayleigh scattering and form a highly reflective cavity. As such, the sensor exhibits a low-finesse Fabry-Perot interferometric spectrum, with a measurable FSR up to a few nanometers wide, and a semi-stochastic spectral envelope due to the random distributions of the nanoparticles.

The sensitivity of the device is experimentally assessed to be 92.5 dB/RIU (average value), similar to the prior high-performance fiber-optic biosensor. Different sensors have been functionalized for CCL5 detection, showing detection limits of 2.86 fM in PBS and 17.6 aM in serum, hence compliant with the best fiber-optic biosensors reported so far. The specificity and reproducibility of the sensing device have been assessed.

The results obtained pave the way for CCL5 real-time detection with a compact sensor, having outstanding biological performance compatible with ultralow-limit detection, suitability for operation in low-abundance analytes, and low-cost disposable operation due to the simplicity of fabrication.

Funding

The research was funded by Nazarbayev University, under grants SMARTER (code: 091019CRP2117), EPICGuide (code: 240919FD3908), M2O-DISK (code: 20122022FD4134), code 021220FD4451, and grant number 021220FD2551.

CRediT authorship contribution statement

Aida Rakhimbekova: Conceptualization, Methodology, Validation, Formal analysis, Writing – original draft, Writing – review & editing. **Kuanysh Seitkamal:** Methodology, Validation, Resources, Writing – original draft, Writing – review & editing. **Baizak Kudaibergenov:** Methodology, Validation, Writing – review & editing. **Faisal Nazir:** Methodology, Formal analysis, Writing – review & editing. **Tri Pham:** Methodology, Formal analysis, Supervision, Writing – original draft, Writing – review & editing, Funding acquisition. **Wilfried Blanc:** Resources, Writing – review & editing. **Luca Vangelista:** Conceptualization, Supervision, Writing – review & editing, Funding acquisition. **Daniele Tosi:** Conceptualization, Methodology, Formal analysis, Data curation, Supervision, Writing – original draft, Writing – review & editing, Funding acquisition.

Declaration of Competing Interest

The authors declare that they have no known competing financial interests or personal relationships that could have appeared to influence the work reported in this paper.

Data availability

Data will be made available on request.

Appendix A. Supplementary data

Supplementary data to this article can be found online at https://doi.org/10.1016/j.optlastec.2023.109953.

References

[1] T. Porstmann, S.T. Kiessig, Enzyme immunoassay techniques an overview, J. Immunol. Methods 150 (1992), https://doi.org/10.1016/0022-1759(92)90061-W.
[2] B. Kaur, S. Kumar, B.K. Kaushik, Recent advancements in optical biosensors for cancer detection, Biosens. Bioelectron. 197 (2022), https://doi.org/10.1016/j.bios.2021.113805.
[3] R. Biswas, Catheter like U-shaped fiber as a probe for oral cancer, Biosens Bioelectron X. 11 (2022), 100181, https://doi.org/10.1016/j.biosx.2022.100181.
[4] M. Loyez, J.C. Larrieu, S. Chevineau, M. Remmelink, D. Leduc, B. Bondue, P. Lambert, J. Devière, R. Wattiez, C. Caucheteur, In situ cancer diagnosis through online plasmonics, Biosens. Bioelectron. 131 (2019), https://doi.org/10.1016/j.bios.2019.01.062.
[5] K.C. Liao, T. Hogen-Esch, F.J. Richmond, L. Marcu, W. Clifton, G.E. Loeb, Percutaneous fiber-optic sensor for chronic glucose monitoring in vivo, Biosens. Bioelectron. 23 (2008), https://doi.org/10.1016/j.bios.2008.01.012.

[6] A.B. Socorro-Leránoz, D. Santano, I. Del Villar, I.R. Matias, Trends in the design of wavelength-based optical fibre biosensors (2008–2018), Biosens Bioelectron X. 1 (2019), https://doi.org/10.1016/j.biosx.2019.100015.

[7] A.K. Sharma, R. Jha, B.D. Gupta, Fiber-optic sensors based on surface plasmon resonance: A comprehensive review, IEEE Sens. J. 7 (2007), https://doi.org/10.1109/JSEN.2007.897946.

[8] R. Bandaru, M. Divagar, S. Khanna, C.G. Danny, S. Gupta, V. Janakiraman, S. VVR, U-bent fiber optic plasmonic biosensor platform for ultrasensitive analyte detection, Sens Actuators B Chem. 321 (2020), https://doi.org/10.1016/j.snb.2020.128463.

[9] J.S. Paiva, P.A.S. Jorge, R.S.R. Ribeiro, M. Balmaña, D. Campos, S. Mereiter, C. Jin, N.G. Karlsson, P. Sampaio, C.A. Reis, J.P.S. Cunha, iLoF: An intelligent Lab on Fiber Approach for Human Cancer Single-Cell Type Identification, Sci. Rep. 10 (2020), https://doi.org/10.1038/s41598-020-59661-5.

[10] C. Leitão, S.O. Pereira, C. Marques, N. Cennamo, L. Zeni, M. Shaimerdenova, T. Ayupova, D. Tosi, Cost-Effective Fiber Optic Solutions for Biosensing, Biosensors (Basel). 12 (2022) 575, https://doi.org/10.3390/bios12080575.

[11] J. Lao, L. Han, Z. Wu, X. Zhang, Y. Huang, Y. Tang, T. Guo, Gold Nanoparticle-Functionalized Surface Plasmon Resonance Optical Fiber Biosensor. In Situ Detection of Thrombin with 1 n·M Detection Limit, J. Lightwave Technol. 37 (2019), https://doi.org/10.1109/JLT.2018.2822827.

[12] M. Lobry, D. Lahem, M. Loyez, M. Debliquy, K. Chah, M. David, C. Caucheteur, Non-enzymatic D-glucose plasmonic optical fiber grating biosensor, Biosens. Bioelectron. 142 (2019), https://doi.org/10.1016/j.bios.2019.111506.

[13] F. Esposito, L. Sansone, A. Srivastava, F. Baldini, S. Campopiano, F. Chiavaioli, M. Giordano, A. Giannetti, A. Iadicicco, Long period grating in double cladding fiber coated with graphene oxide as high-performance optical platform for biosensing, Biosens. Bioelectron. 172 (2021), https://doi.org/10.1016/j.bios.2020.112747.

[14] F. Esposito, (INVITED)Chemical sensors based on long period fiber gratings: A review, Results in Optics. 5 (2021), https://doi.org/10.1016/j.rio.2021.100196.

[15] S. Choudhary, F. Esposito, L. Sansone, M. Giordano, S. Campopiano, A. Iadicicco, Lossy mode resonance sensors in uncoated optical fiber, IEEE Sens. J. (2023), https://doi.org/10.1109/JSEN.2023.3280675.

[16] C. Caucheteur, T. Guo, F. Liu, B.O. Guan, J. Albert, Ultrasensitive plasmonic sensing in air using optical fibre spectral combs, Nat. Commun. 7 (2016), https://doi.org/10.1038/ncomms13371.

[17] T. Guo, F. Liu, B.O. Guan, J. Albert, Tilted fiber grating mechanical and biochemical sensors, Opt. Laser Technol. 78 (2016), https://doi.org/10.1016/j.optlastec.2015.10.007.

[18] Y. Ran, J. Long, Z. Xu, Y. Yin, D. Hu, X. Long, Y. Zhang, L. Liang, H. Liang, B. O. Guan, Harmonic optical microfiber Bragg grating immunosensor for the accelerative test of cardiac biomarker (cTn-I), Biosens. Bioelectron. 179 (2021), https://doi.org/10.1016/j.bios.2021.113081.

[19] Y. Huang, Z. Tian, L.-P. Sun, D. Sun, J. Li, Y. Ran, B.-O. Guan, High-sensitivity DNA biosensor based on optical fiber taper interferometer coated with conjugated polymer tentacle, Opt. Express 23 (2015), https://doi.org/10.1364/oe.23.026962.

[20] S. Gao, L.-P. Sun, J. Li, L. Jin, Y. Ran, Y. Huang, B.-O. Guan, High-sensitivity DNA biosensor based on microfiber Sagnac interferometer, Opt. Express 25 (2017), https://doi.org/10.1364/oe.25.013305.

[21] D. Sun, Y. Fu, Y. Yang, Label-free detection of breast cancer biomarker using silica microfiber interferometry, Opt. Commun. 463 (2020), https://doi.org/10.1016/j.optcom.2020.125375.

[22] D. Tosi, M. Shaimerdenova, M. Sypabekova, T. Ayupova, Minimalistic design and rapid-fabrication single-mode fiber biosensors: Review and perspectives, Opt. Fiber Technol. 72 (2022), 102968, https://doi.org/10.1016/j.yofte.2022.102968.

[23] A. Bekmurzayeva, Z. Ashikbayeva, N. Assylbekova, Z. Myrkhiyeva, A. Dauletova, T. Ayupova, M. Shaimerdenova, D. Tosi, Ultra-wide, attomolar-level limit detection of CD44 biomarker with a silanized optical fiber biosensor, Biosens. Bioelectron. 208 (2022), https://doi.org/10.1016/j.bios.2022.114217.

[24] W. Blanc, Z. Lu, T. Robine, F. Pigeonneau, C. Molardi, D. Tosi, Nanoparticles in optical fiber, issue and opportunity of light scattering [Invited], Opt. Mater. Express 12 (2022) 2635, https://doi.org/10.1364/OME.462822.

[25] A. Beisenova, A. Issatayeva, I. Iordachita, W. Blanc, C. Molardi, D. Tosi, Distributed fiber optics 3D shape sensing by means of high scattering NP-doped fibers simultaneous spatial multiplexing, Opt. Express 27 (2019), https://doi.org/10.1364/oe.27.022074.

[26] M. Sypabekova, A. Aitkulov, W. Blanc, D. Tosi, Reflector-less nanoparticles doped optical fiber biosensor for the detection of proteins: Case thrombin, Biosens. Bioelectron. 165 (2020), https://doi.org/10.1016/j.bios.2020.112365.

[27] M. Shaimerdenova, T. Ayupova, Z. Ashikbayeva, A. Bekmurzayeva, W. Blanc, D. Tosi, Reflector-Less Shallow-Tapered Optical Fiber Biosensors for Rapid Detection of Cancer Biomarkers, J. Lightwave Technol. (2022) 1–10.

[28] Z. Ashikbayeva, A. Aitkulov, M. Jelbuldina, A. Issatayeva, A. Beisenova, C. Molardi, P. Saccomandi, W. Blanc, V.J. Inglezakis, D. Tosi, Distributed 2D temperature sensing during nanoparticles assisted laser ablation by means of high-scattering fiber sensors, Sci. Rep. 10 (2020), https://doi.org/10.1038/s41598-020-69384-2.

[29] F.R. Balkwill, The chemokine system and cancer, J. Pathol. 226 (2012), https://doi.org/10.1002/path.3029.

[30] D. Aldinucci, C. Borghese, N. Casagrande, The ccl5/ccr5 axis in cancer progression, Cancers (Basel). 12 (2020), https://doi.org/10.3390/cancers12071765.

[31] D. Aldinucci, N. Casagrande, Inhibition of the CCL5/CCR5 axis against the progression of gastric cancer, Int. J. Mol. Sci. 19 (2018), https://doi.org/10.3390/ijms19051477.

[32] S. Svensson, A. Abrahamsson, G.V. Rodriguez, A.K. Olsson, L. Jensen, Y. Cao, C. Dabrosin, CCL2 and CCL5 are novel therapeutic targets for estrogen-dependent breast cancer, Clin. Cancer Res. 21 (2015), https://doi.org/10.1158/1078-0432.CCR-15-0204.

[33] L. Xia, X. Zhu, L. Zhang, Y. Xu, G. Chen, J. Luo, EZH2 enhances expression of CCL5 to promote recruitment of macrophages and invasion in lung cancer, Biotechnol. Appl. Biochem. 67 (2020), https://doi.org/10.1002/bab.1875.

[34] R. Huang, S. Wang, N. Wang, Y. Zheng, J. Zhou, B. Yang, X. Wang, J. Zhang, L. Guo, S. Wang, Z. Chen, Z. Wang, S. Xiang, CCL5 derived from tumor-associated macrophages promotes prostate cancer stem cells and metastasis via activating β-catenin/STAT3 signaling, Cell Death Dis. 11 (2020), https://doi.org/10.1038/s41419-020-2435-y.

[35] S.K. Singh, M.K. Mishra, I.E.A. Eltoum, S. Bae, J.W. Lillard, R. Singh, CCR5/CCL5 axis interaction promotes migratory and invasiveness of pancreatic cancer cells, Sci. Rep. 8 (2018), https://doi.org/10.1038/s41598-018-19643-0.

[36] M. Goto, M. Liu, Chemokines and their receptors as biomarkers in esophageal cancer, Esophagus 17 (2020), https://doi.org/10.1007/s10388-019-00706-8.

[37] Z.A. Dehqanzada, C.E. Storrer, M.T. Hueman, R.J. Foley, K.A. Harris, Y.H. Jama, C. D. Shriver, S. Ponniah, G.E. Peoples, Assessing serum cytokine profiles in breast cancer patients receiving a HER2/neu vaccine using Luminex® technology, Oncol. Rep. 17 (2007), https://doi.org/10.3892/or.17.3.687.

[38] H. Sugasawa, T. Ichikura, H. Tsujimoto, M. Kinoshita, D. Morita, S. Ono, K. Chochi, H. Tsuda, S. Seki, H. Mochizuki, Prognostic significance of expression of CCL5/RANTES receptors in patients with gastric cancer, J. Surg. Oncol. 97 (2008), https://doi.org/10.1002/jso.20984.

[39] A. Smeets, B. Brouwers, S. Hatse, A. Laenen, R. Paridaens, G. Floris, H. Wildiers, M.-R. Christiaens, Circulating CCL5 Levels in Patients with Breast Cancer: Is There a Correlation with Lymph Node Metastasis? ISRN Immunology. 2013 (2013) https://doi.org/10.1155/2013/453561.

[40] Y. Fujimoto, N. Inoue, K. Morimoto, T. Watanabe, S. Hirota, M. Imamura, Y. Matsushita, T. Katagiri, H. Okamura, Y. Miyoshi, Significant association between high serum CCL5 levels and better disease-free survival of patients with early breast cancer, Cancer Sci. 111 (2020), https://doi.org/10.1111/cas.14234.

[41] L. Vangelista, S. Vento, The expanding therapeutic perspective of CCR5 blockade, Front. Immunol. 8 (2018), https://doi.org/10.3389/fimmu.2017.01981.

[42] S. Sakamoto, W. Putalun, S. Vimolmangkang, W. Phoolcharoen, Y. Shoyama, H. Tanaka, S. Morimoto, Enzyme-linked immunosorbent assay for the quantitative/qualitative analysis of plant secondary metabolites, J. Nat. Med. 72 (2018), https://doi.org/10.1007/s11418-017-1144-z.

[43] Y. Gao, Y. Zhou, R. Chandrawati, Metal and Metal Oxide Nanoparticles to Enhance the Performance of Enzyme-Linked Immunosorbent Assay (ELISA), ACS Appl Nano Mater. 3 (2020), https://doi.org/10.1021/acsanm.9b02003.

[44] W. Blanc, V. Mauroy, L. Nguyen, B.N. Shivakiran Bhaktha, P. Sebbah, B.P. Pal, B. Dussardier, Fabrication of rare earth-doped transparent glass ceramic optical fibers by modified chemical vapor deposition, J. Am. Ceram. Soc. 94 (2011), https://doi.org/10.1111/j.1551-2916.2011.04672.x.

[45] W. Blanc, I. Martin, H. Francois-Saint-Cyr, X. Bidault, S. Chaussedent, C. Hombourger, S. Lacomme, P. Le Coustumer, D.R. Neuville, D.J. Larson, T. J. Prosa, C. Guillermier, Compositional Changes at the Early Stages of Nanoparticles Growth in Glasses, J. Phys. Chem. C 123 (2019), https://doi.org/10.1021/acs.jpcc.9b08577.

[46] M. Vermillac, J.F. Lupi, F. Peters, M. Cabié, P. Vennéguès, C. Kucera, T. Neisius, J. Ballato, W. Blanc, Fiber-draw-induced elongation and break-up of particles inside the core of a silica-based optical fiber, J. Am. Ceram. Soc. 100 (2017), https://doi.org/10.1111/jace.14774.

[47] N. Aissaoui, L. Bergaoui, J. Landoulsi, J.F. Lambert, S. Boujday, Silane layers on silicon surfaces: Mechanism of interaction, stability, and influence on protein adsorption, Langmuir 28 (2012), https://doi.org/10.1021/la2036778.

[48] C. Ma, B. Dong, J. Gong, A. Wang, Decoding the spectra of low-finesse extrinsic optical fiber Fabry-Perot interferometers, Opt. Express 19 (2011), https://doi.org/10.1364/oe.19.023727.

[49] D. Tosi, Review and analysis of peak tracking techniques for fiber bragg grating sensors, Sensors (Switzerland). 17 (2017), https://doi.org/10.3390/s17102368.

[50] A. Bekmurzayeva, Z. Ashikbayeva, Z. Myrkhiyeva, A. Nugmanova, M. Shaimerdenova, T. Ayupova, D. Tosi, Label-free fiber-optic spherical tip biosensor to enable picomolar-level detection of CD44 protein, Sci. Rep. 11 (2021), https://doi.org/10.1038/s41598-021-99099-x.

[51] Z. Ashikbayeva, A. Bekmurzayeva, Z. Myrkhiyeva, N. Assylbekova, T.S. Atabaev, D. Tosi, Green-synthesized gold nanoparticle-based optical fiber ball resonator biosensor for cancer biomarker detection, Opt. Laser Technol. 161 (2023), https://doi.org/10.1016/j.optlastec.2023.109136.

[52] Z. Li, C. Liao, D. Chen, J. Song, W. Jin, G.-D. Peng, F. Zhu, Y. Wang, J. He, Y. Wang, Label-free detection of bovine serum albumin based on an in-fiber Mach-Zehnder interferometric biosensor, Opt. Express 25 (2017), https://doi.org/10.1364/oe.25.017105.